Computers, Materials & Continua

Tech Science Press

https://doi.org/10.32604/cmc.2026.078880

ARTICLE

Effects of Graphene Defects on Evolution of Dislocations and Pores in Graphene/Al Composites: A Molecular Dynamics Study

Junzhe Zhao[1,2], Wencan Zhu[1,3], Qiang Wang[1], Hui Chen[2], Yan Liu[2], Kaihong Zheng[3] and Zhibo Zhang[2,3,*]

[1]State Key Laboratory of Metaslele Materials Science and Technology and Key Laboratory for Microstructural Material Physics of Hebei Province, School of Science, Yanshan University, Qinhuangdao, China

[2]School of Materials Science and Engineering, Southwest Jiaotong University, Chengdu, China

[3]National Engineering Research Center of Powder Metallurgy of Titanium & Rare Metals, Guangdong Provincial Key Laboratory of Metal Toughening Technology and Application, Institute of New Materials, Guangdong Academy of Sciences, Guangzhou, China

*Corresponding Author: Zhibo Zhang. Email: zhibo_zhang88@sina.com

Received: 09 January 2026; Accepted: 22 April 2026; Published: 15 June 2026

ABSTRACT: Vacancy defects in graphene are inevitably introduced during the fabrication of graphene-reinforced metal matrix composites through mechanical processing, chemical reactions, or in-service environmental exposure. Despite their prevalence, the precise atomic-scale impact of these vacancies on dislocation motion, strengthening mechanisms, and failure behavior remains incompletely understood. To address this gap, we employ molecular dynamics simulations to construct aluminum-graphene interface models featuring systematically varied vacancy defect concentrations, enabling a detailed investigation of dislocation–interface interactions and the underlying reinforcement and failure mechanisms under shear deformation. Compared to pristine graphene, interfaces containing vacancy defects exhibit significantly enhanced out-of-plane buckling when dislocations impinge upon the interface, disrupting the periodicity of buckling waves, reducing interfacial stability, and ultimately degrading the overall mechanical performance of the composite. The buckling amplitude shows a positive correlation with the contact area between vacancies and the dislocation slip plane, highlighting the role of localized defect-dislocation overlap in amplifying structural perturbations. During shear loading, vacancy defects markedly impair load transfer efficiency across the aluminum–graphene interface, precipitating pronounced stress concentrations that nucleate preferentially at the edges of the atomic voids. Consequently, the shear strength of the graphene-reinforced aluminum composite undergoes a monotonic decrease as the defect area fraction increases. Quantitatively, as the defect area fraction rises from 1.24% to 13.8%, the shear strength declines markedly by approximately 14%–15%. Beyond the 13.8% threshold, the mechanical response deteriorates precipitously, characterized by disordered buckling waves localized near the voids, which act as precursors to premature interfacial fracture. These findings provide a theoretical basis for the design optimization of aluminum-graphene composites in experiments.

KEYWORDS: Molecular dynamics simulation; mechanical properties; dislocation-interface interaction; shear deformation; vacancy defects

1 Introduction

Graphene-reinforced metal matrix composites exhibit excellent structural, mechanical, and tribological properties, with broad applications in aerospace, automotive, electronics, and biomedical fields [1–5]. However, during the fabrication of these composites, mechanical actions such as friction and stirring, as

well as certain chemical reactions, inevitably damage the graphene structure [6], resulting in surface defects. Beyond fabrication, in-service exposure to irradiation and chemical corrosion can also generate graphene surface defects [7]. In the context of metal matrix composites, graphene surface defects are typically classified by morphology into vacancy defects, line defects, and pore defects [8,9]. Vacancy defects can be formed by rotating a C-C bond by 90°, transforming four hexagons into two pentagons and two heptagons [10], if defect spacing is uniform, the strength of tilted grain boundaries increases with the square of the tilt angle [11]. Stone-Wales defects introduce pentagon-heptagon pairs, creating local curvature that increasing surface reactivity and roughness. This significantly enhances interfacial bonding and electron transfer with polymers or metals, improving adhesion and overall composite performance [12]. Additionally, atomic aggregation near vacancies can form defect bubbles in graphene, which polymerize into defect ridges and further develop into planar defect bands [9]. Plasma treatment produces 5–10 nm nanopores on the basal plane of P-GO, yielding higher strength enhancement and improved interface stability compared to untreated graphene composites [11]. Controlled nanopores (with tunable size and density) enhance interfacial adhesion and load transfer efficiency by increasing specific surface area and providing mechanical anchoring, improving mechanical synergy in composites [13]. Thus, graphene vacancies significantly influence the performance of metal matrix composites, including strengthening mechanisms and mechanical properties, attracting considerable attention.

Larger-area defects on graphene surfaces profoundly affect the mechanical properties of metal matrix graphene composites. Experimental results indicate that pentagons (positive curvature defects) and heptagons (negative curvature defects) in graphene cause local stress concentrations, facilitating plastic deformation (dislocation slip) and reducing service life [14]. Defective graphene exhibits significantly higher shear strain accommodation and strain stiffening capabilities during deformation, resisting interlayer shear/strain localization [15], while increasing its content in Al composites enhances load transfer efficiency and thereby significantly improves the yield strength and ultimate tensile strength [16]. In simulation calculations, defective graphene enhances the Cu–C interfacial bonding effect through strong Cu–C interactions at the defect sites, thereby improving the mechanical properties of the material [17]. But smaller defects on graphene surfaces may expand into larger pore defects under stress loading, further diminishing composite performance [18]. Numerous studies indicate that graphene vacancies critically impact metal matrix composite performance, but the effect of graphene defect on dislocations interacting with interface has not been fully revealed at the atomic scale, severely hindering structural design and performance optimization of graphene-reinforced metal matrix composites.

Molecular dynamics (MD) simulations have achieved substantial progress in elucidating the mechanisms of dislocation-interface interactions and uncovering associated strengthening and failure processes. Jin et al. investigated dislocation transmission across grain boundaries using MD simulations of perfect lattice screw dislocations interacting with {111} coherent twin boundaries (CTBs). They found that screw dislocations approaching a coherent boundary from one side can either transmit into the adjacent twin grain by cross-slip across the boundary or dissociate within the boundary plane [19]. Wang focused on edge dislocation interactions with pairs of single-layer graphene nanosheets (GNS) oriented on different crystal planes, examining the mechanical response and dislocation evolution in graphene/iron composites during deformation. Their results showed that edge dislocations experience the strongest blocking effect when the GNS are parallel to the (111) plane [20]. Zhu et al. conducted MD tensile simulations on aluminum-graphene composites with varying aluminum crystal orientations, demonstrating that interfaces formed between the Al (111) face and graphene yield the highest composite strength, followed by Al (110) and then Al (100) [21]. Qiu et al. employed MD to explore size effects in graphene-reinforced aluminum matrix composites, attributing these effects to competing strengthening and softening mechanisms at dislocation-interface

interactions [22], while also clarifying the influence of interface characteristics and reinforcement shape on dislocation motion and strengthening in silicon-reinforced aluminum composites [23–25]. Furthermore, MD simulations have revealed the impact of Al/Si interfaces on friction force and coefficient during tribological processes, along with the associated microstructural evolution [26], showing that reinforcements elevate stress levels at interfaces and grain boundaries, thereby enhancing boundary stability and conferring benefits for friction reduction and wear resistance [27].

Therefore, this study employs molecular dynamics simulations to construct aluminum-graphene interface models with various vacancy defects, systematically examining the effects of graphene vacancy defects on dislocation-interface interactions and strengthening and failure mechanisms in shear deformation. The work investigates the deformation behavior of single dislocations slipping to the graphene-aluminum (111) interface and the shear deformation process in graphene-reinforced aluminum composites, revealing that vacancy-containing graphene interfaces reduce interface stability and thus mechanical performance, with buckling deformation degree positively correlating with the contact area between vacancies and dislocation slip;during shear deformation, graphene vacancies weaken load transfer efficiency, reducing strength in graphene-reinforced aluminum matrix composites, with disordered buckling waves and peaks-valleys concentrated near pores inducing early fracture.

2 Computational Methods

All simulations were performed using LAMMPS [28] with atomic configurations visualized and analyzed in OVITO [29] employing common neighbor analysis (CNA) and dislocation extraction algorithm (DXA) [30,31]. A time step of 1 fs was used. Prior to production runs, systems were energy-minimized via conjugate gradient descent and relaxed for 50 ps under the NPT ensemble to achieve equilibrium. During relaxation, several atomic layers on the left side (parallel to the Y-axis) were fixed as a rigid region. To drive dislocation slip toward the aluminum-graphene interface, opposing shear strains parallel to the Z-direction were applied to the upper and lower halves of the model along the Y-axis: a strain in the opposite direction was imposed on the upper half, while a constant strain parallel to the Z-axis–aligned with the ($[\bar{1}\bar{1}1]$ $[1\bar{1}0]$) slip system–was applied to the lower half. Temperature was maintained at 0.1 K to suppress thermal fluctuations (e.g., thermally driven lattice slip) and facilitate the detection of crystal defects such as dislocations and phase transformations [24–27]. The applied strain rate in this MD study (10-3 ps-1) is significantly higher than those in typical experimental conditions, a intrinsic limitation of molecular dynamics simulations arising from the femtosecond timescale of atomic vibrations [32,33].

Carbon–carbon interactions were described by the adaptive intermolecular reactive empirical bond order (AIREBO) potential [34], aluminum–aluminum interactions by an embedded atom method (EAM) potential [31], and aluminum–carbon interactions by a Lennard-Jones (LJ) potential with well depth 3.0135 Å and cutoff 0.0351 eV [35]. In this study, various defects were broadly classified into vacancy defects (absence of individual atoms or small clusters), pore defects (larger multivacancy clusters exceeding 5 Å), and line defects.

2.1 Dislocation Motion Simulations

As depicted in Fig. 1, aluminum/graphene/aluminum sandwich composite models were constructed using LAMMPS. The aluminum crystals were face-centered cubic (FCC) with a lattice constant of 4.0495 Å. Dark gray atoms represent aluminum, while black atoms denote carbon in graphene;the models contained approximately 180,000 atoms in total. Non-periodic shrink-wrapped boundary conditions were employed in the x and y directions, with periodic boundaries applied in the z direction. A full screw dislocation with Burgers vector ($b = \frac{a_0}{2}\langle 110\rangle$) parallel to the z-axis and line direction along was introduced at the midpoint of the left aluminum slab (along the y-direction) using Atomsk. Due to the periodic boundary condition in

the z-direction, the dislocation line can be considered infinitely long within the y–z plane. This full screw dislocation ($\frac{a_0}{2}$<110>) was utilized for molecular dynamics simulations investigating single dislocation slip toward the aluminum-graphene interface. The crystallographic orientations along the x, y, and z axes were [112], [$\bar{1}\bar{1}$1], and [1$\bar{1}$0], respectively.

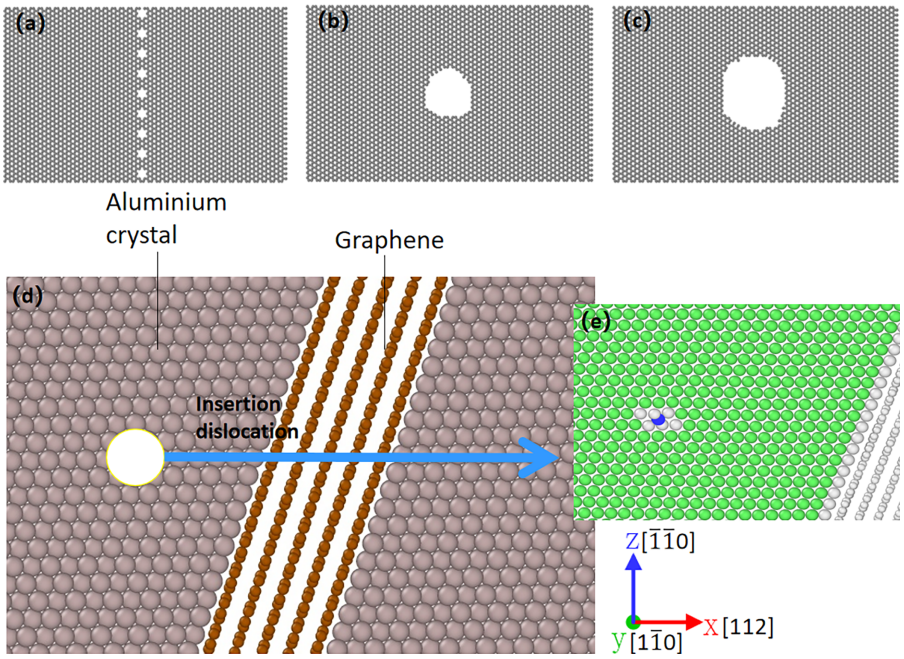

Figure 1: Different types of graphene defects introduced directly opposite the dislocation slip path. (**a**) line defects (isolated small clusters in line); (**b**) small pore defects (multivacancy clusters); (**c**) large pore defects (extended multivacancy pores); (**d**) construction of the Al-graphene-Al sandwich composite containing a single dislocation; (**e**) the full screw dislocation introduced in the left Al slab.

As illustrated in Fig. 1a–c, we introduced different defect types into the graphene sheet directly opposite the dislocation path. Fig. 1a shows line defects (one-dimensional topological defects) formed by periodically repeating pentagon–octagon–pentagon (5-8-5) sp^2-hybridized rings seamlessly embedded in the pristine honeycomb lattice. These defects exhibit perfect atomic coordination without dangling bonds and well-defined metallic character, offering an ideal platform for atomic-scale engineering of low-resistance, stable electrical contacts [36]. Fig. 1b,c depicts nanopores of varying area, typically produced experimentally by focused ion beam (FIB) milling to yield diameters of 100–400 nm. Such pores disrupt phonon transport symmetry and alter the temperature dependence of thermal conductivity [9]. Fig. 1d,e illustrates the construction of the aluminum-graphene composite containing a single dislocation and the built perfect screw dislocation.

For shear failure studies, we constructed additional models containing graphene with pore area fractions of 1.24%, 3.72%, 8.10%, 13.8%, 16.6%, and 20.3% (Fig. 2a–f). The specific defective region fractions simulated in this study (e.g., 13.8%) correspond to macroscopic physical dimensions (defective area occupying ~13.8% of the total sample). Such pores defects can be achieved using synthesis techniques such as focused ion beam (FIB) milling or chemical oxidation [37,38].

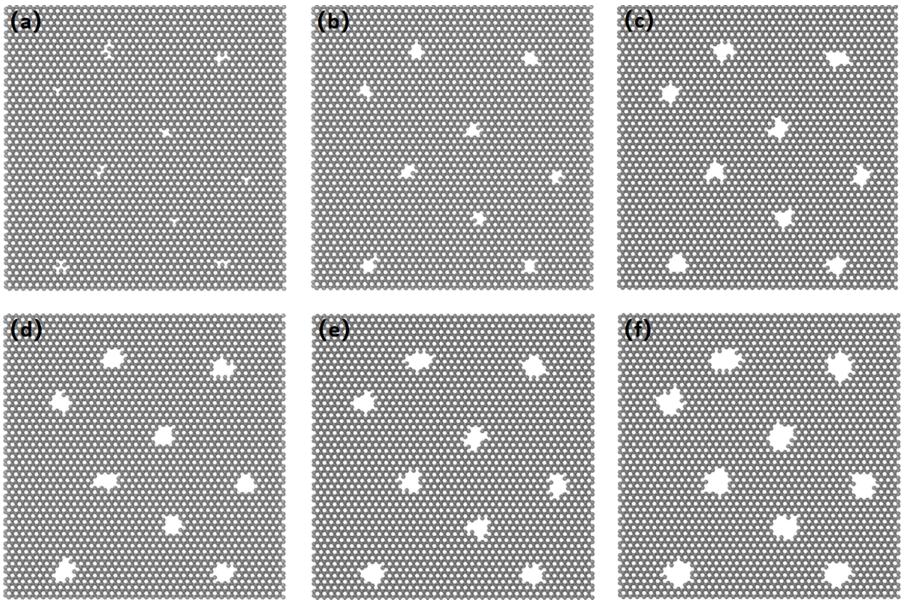

Figure 2: Graphene with different defect areas within the composite material. Models of graphene sheets containing various defect areas were prepared. These graphene sheets were then inserted into the aluminum crystal matrix to create aluminum-graphene composite models. These composites share the same aluminum matrix volume but contain graphene with different defect areas. The defect areas (void areas) for the graphene sheets shown in (**a**–**f**) are 1.24%, 3.72%, 8.10%, 13.8%, 16.6%, and 20.3%, respectively.

2.2 Macroscopic Shear Response

To investigate the performance of aluminum-graphene composites under conditions representative of in-service loading, we employed infinite shear models, which are widely utilized to probe the shear response of materials [39].

The pure aluminum single-crystal model and the sandwich structure model (Fig. 3a,b), wherein the sandwich structure model employs an aluminum/graphene/aluminum three-layer sandwich design, with the graphene sheet oriented parallel to the x–y plane and aligned uniformly to optimize its load-bearing capacity [40]. Aluminum atoms are depicted in green and carbon atoms in gray. The *x*, *y*, and *z* axes correspond to the [100], [010], and [001] crystallographic directions of the face-centered cubic aluminum lattice, respectively.

Shear loading was applied by imposing opposing displacements along the *x*-direction on the upper and lower portions of the model (Fig. 3c,d). Prior to deformation, each system was energy-minimized and subsequently relaxed for 100 ps under the NPT ensemble at 300 K to achieve equilibrium, with periodic boundary conditions applied in all directions. Shear deformation was then performed under the NVT ensemble at 300 K, with a constant strain rate of 10-3 ps-1 implemented via strain increments applied every 1000 time steps. The engineering shear strain γ was calculated as $\gamma = \delta x/Ly$, where δx represents the relative displacement along the *x*-direction and Ly is the model dimension along the *y*-direction.

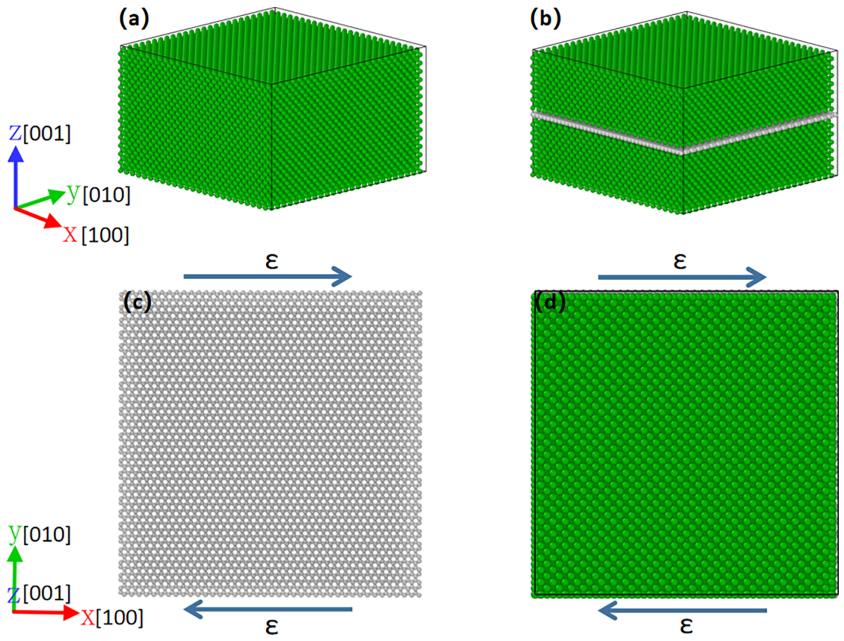

Figure 3: (**a**) Pure aluminum single crystal, where the *X*, *Y*, and *Z* directions represent the crystal orientations [001], [010], and [001], respectively; (**b**) Model of the aluminum-graphene composite material, obtained by removing two atomic layers of aluminum from the middle of the pure aluminum single crystal (**a**) and inserting a layer of graphene; (**c**) The graphene within the composite material (**b**), with the zigzag chiral direction along the *x*-axis and the armchair chiral direction along the *y*-axis; (**d**) Top view of the aluminum-graphene composite material, where the blue arrows parallel to the *x*-axis indicate the direction of applied strain.

3 Results and Discussion

3.1 Influence of Graphene Vacancies on Dislocation-Interface Interactions

Following relaxation, the initial full screw dislocation dissociated into two partial dislocations with Burgers vectors $\frac{a_0}{6} < 2\bar{1}1 >$ and $\frac{a_0}{6} < 1\overline{21} >$ (Fig. 4), reflecting the lower energy of the extended configuration [18].

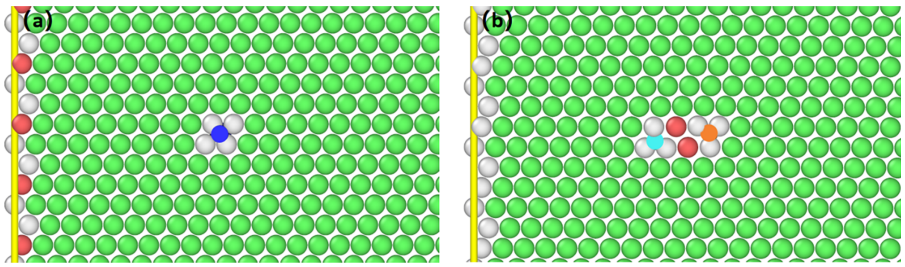

Figure 4: (**a**) The full screw dislocation ($\frac{a_0}{2} < 1\bar{1}0 >$) initially present within the aluminum crystal at the early stage of model construction, shown in blue; (**b**) After relaxation, the full screw dislocation has dissociated into two partial dislocations: $\frac{a_0}{6} < 2\bar{1}1 >$ (orange) and $\frac{a_0}{6} < 1\overline{21} >$ (cyan). The yellow line on the left side in (**a**,**b**) represents the frame border.

The interaction between dislocations and the pristine graphene interface is illustrated in Fig. 5a–d. Under applied shear stress, two partial screw dislocations first coalesce into a perfect screw dislocation (Fig. 5a), which subsequently glides along the slip plane. As part of the perfect dislocation has already

terminated at the aluminum crystal boundary, the dislocation undergoes re-dissociation, leaving only the trailing $\frac{a_0}{6} < 1\bar{2}1 >$ partial screw dislocation (Fig. 5b). The leading segment of the perfect dislocation then impinges upon the Al–graphene interface, where the dislocation temporarily vanishes once fully transmitted across the boundary (Fig. 5c). However, owing to the pronounced lattice distortion within the aluminum matrix, the exceptional toughness of graphene, and its strong resistance to dislocation motion, the graphene at the interface acts as a dislocation source. This process nucleates new dislocations at the boundary, which subsequently accumulate to form a stable dislocation lock (Fig. 5d). Such interfacial dislocation locking significantly enhances the mechanical performance of Al–graphene composites.

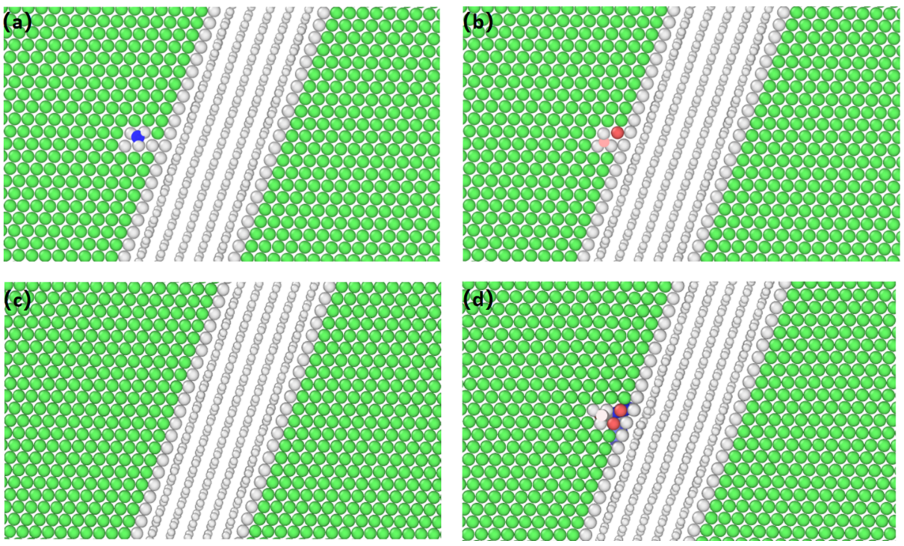

Figure 5: Deformation behavior during dislocation entering the interface. Larger spheres represent Al atoms and smaller spheres represent C atoms. Blue atoms mark the full screw dislocation ($\frac{a_0}{2} < 1\bar{1}0 >$), pink atoms represent partial dislocations $\frac{a_0}{6} < 1\bar{2}1 >$, and red atoms represent other dislocations. (**a**) atomic configuration as the dislocation approaches the interface; (**b**) entry of the dislocation core into the interface; (**c**) instantaneous configuration after the dislocation continues to traverse the interface; (**d**) reaction or dissociation of the dislocation at the interface, forming two separated cores.

As shown in Fig. 6, during the process of dislocation transmission into the interface, graphene undergoes buckling deformation induced by the plastic strain associated with dislocation glide in the aluminum matrix. Owing to the high ductility of graphene and its relatively large interlayer spacing, the buckling displacement at the interface center propagates symmetrically toward both sides, effectively dissipating the kinetic energy and stress shock generated by dislocation impingement at the interface. Notably, pronounced buckling occurs only in the graphene layerinterface region. This localized deformation originates at the site of dislocation–graphene interaction and subsequently spreads outward, forming periodic buckling waves that buffer along the direction parallel to the Al (111) plane.

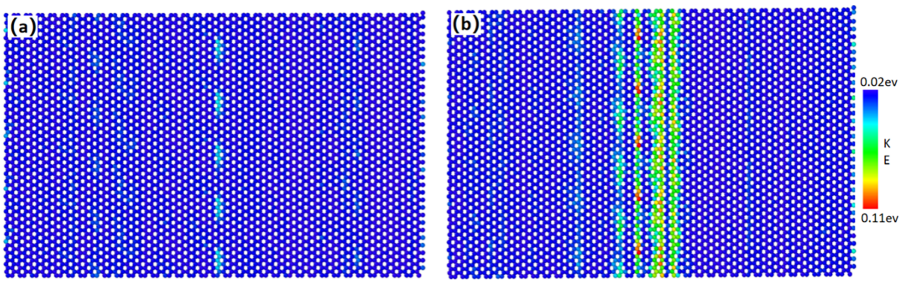

Figure 6: Propagation of graphene buckling waves during the stage of dislocation entering the interface. The colors indicate atomic kinetic energy, ranging from blue (representing low kinetic energy regions) to red (high kinetic energy regions). (**a**) Atomic configuration at the moment when the dislocation just enters the interface, where buckling waves have not yet propagated significantly; (**b**) Instantaneous snapshot after the dislocation continues to enter the interface, with buckling waves propagating along the interface direction.

The influence of graphene defects on dislocation–interface interactions is illustrated in Fig. 7. When a perfect dislocation fully impinges upon the interface, the extent of buckling deformation in pristine graphene is compared with that in defective graphene. By comparing the deviation from a reference line representing the equilibrium interatomic distance, the magnitude of out-of-plane displacement in defective graphene can be more clearly observed. At the initial stage of dislocation entry, pristine graphene exhibits only minor buckling, whereas defective graphene surfaces display pronounced deformation. The presence of defects disrupts the structural symmetry and integrity of graphene; the larger the defect area in contact with the dislocation, the greater the structural perturbation and the stronger the impact on buckling behavior. Consequently, during dislocation transmission across the Al–graphene interface, defective graphene exhibits significantly larger buckling waves compared to pristine graphene in Al–graphene composites.

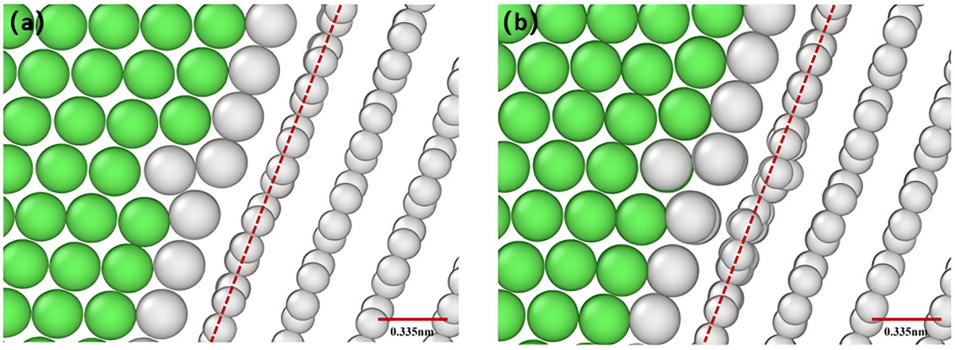

Figure 7: (Continued)

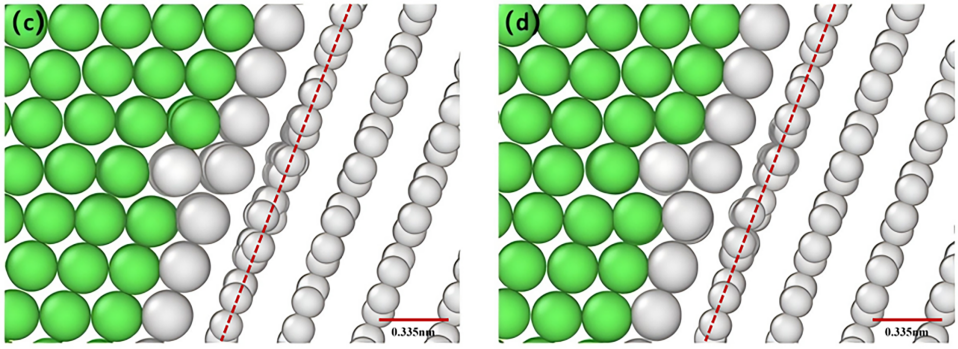

Figure 7: Buckling deformation generated on different graphene surfaces at the moment when the dislocation fully enters the graphene interface. Larger spheres represent Al atoms, and smaller spheres represent C atoms. (**a**) buckling deformation of pristine graphene; (**b**) buckling deformation of graphene with line defects; (**c**) buckling deformation of graphene with small pore defects; (**d**) buckling deformation of graphene with large pore defects. The red dashed line represents the buckling deformation standard comparison line.

Among the defective configurations, graphene containing line defects shows the most severe buckling deformation (Fig. 7b), followed by graphene with large vacancy defects (Fig. 7d), while graphene with small vacancy defects exhibits the least deformation (Fig. 7c). Although the surface defect area of graphene with large vacancies exceeds that of line-defective graphene, its direct contact area with the dislocation glide path is smaller, resulting in reduced buckling amplitude. This observation indicates that buckling waves are more strongly correlated with the contact area between dislocations and graphene defects than with the absolute defect area. When dislocations reach the interface, localized stress fields are generated within both the aluminum matrix and graphene. A larger contact area amplifies the stress concentration at the defect site, thereby inducing greater buckling deformation. Such enhanced deformation significantly influences the mechanical response and strength of Al–graphene composites.

The instantaneous entry of a single dislocation into the interface induces significantly larger fluctuations in defective graphene compared to pristine graphene (Fig. 8). (The central region marks the dislocation–interface contact site, with color brightness representing the kinetic energy of graphene atoms). The red dashed line denotes the contact interface between the dislocation and the defect upon entering the interface. When the dislocation core reaches the graphene interface, its localized stress field is transmitted across the boundary. In the presence of defects such as vacancies, grain boundaries, or waves, the local stiffness of graphene is reduced, leading to pronounced stress concentration around the defect sites. These intensified fluctuations diminish the reinforcing effect of graphene on aluminum, thereby compromising the mechanical performance of Al–graphene composites.

For vacancy defects of different sizes, larger defect areas produce greater fluctuations at the moment of dislocation entry. However, graphene with line defects–despite having a smaller defect area–exhibits even stronger fluctuations when the defect is in direct contact with the dislocation glide path. The contact area between dislocations and defects is proportional to the length occupied by defects on the red dashed line, respectively 62% (line defects), 24% (small pore defects) and 37% (large pore defects). This indicates that the amplitude of graphene fluctuations is governed primarily by the contact area between dislocations and defects rather than the absolute defect size.

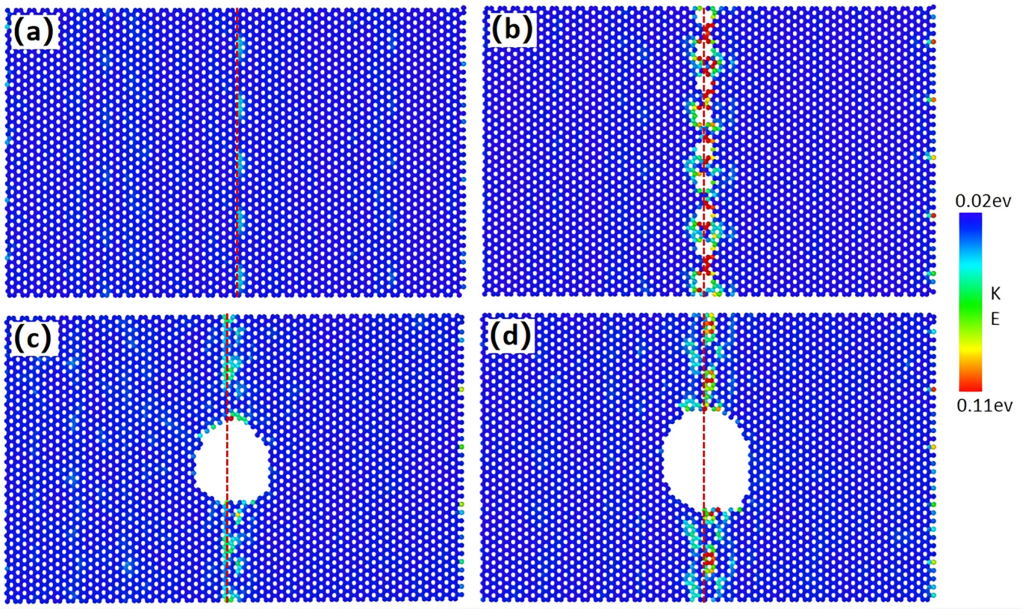

Figure 8: Kinetic energy of surface atoms in graphene at the moment the dislocation enters the Al-graphene interface, red atoms indicate high kinetic energy, while blue atoms represent low kinetic energy, red dashed line: the interface between the dislocation and the defect. (**a**) Graphene without defects; (**b**) Graphene containing line defects; (**c**) Graphene containing smaller pore defects; (**d**) Graphene containing larger pore defects.

Comparisons of vibration periods for dislocation-entry waves in different graphene reveal clear regularity in defect-free graphene: λ = 31.42 h. Defective graphene shows weaker periodicity because buckling waves reflect, refract, or mode-convert at defects, disordering overall waves;disordered waves lead to uneven energy dissipation, with partial kinetic energy released as local heat or interface debonding, affecting dislocation kinetic energy unloading and thus material mechanical properties.

3.2 Influence of Graphene Vacancies on Shear Strengthening and Failure

For Al–graphene composites reinforced with defect-free graphene, the entire shear process can be divided into three distinct stages: the elastic stage, the yielding stage, and the failure stage. A key factor underlying the enhanced mechanical performance is the load-transfer mechanism provided by the graphene reinforcement. During the application of shear loading, once the stress is transmitted to the graphene, the internal C–C bonds undergo tensile elongation. This bond stretching enables graphene to effectively bear a substantial portion of the applied load, thereby significantly improving the overall load-bearing capacity of the composite.

Under shear loading, from strain initiation to graphene fracture–spanning elastic to yield stages–graphene buckling waves and borne stress intensify with increasing strain, with carried stress rising. Upon reaching failure, graphene fractures entirely, with borne stress dropping instantly to low levels. Under shear, out-of-plane graphene displacement is constrained by the aluminum matrix, further enhancing composite strength (Fig. 9a–c). Importantly, during shear loading, the out-of-plane displacement of graphene is constrained by the surrounding aluminum matrix. This restriction suppresses excessive buckling and contributes to enhanced strength of the composite, underscoring the critical role of interfacial confinement in the mechanical reinforcement of Al–graphene systems (Fig. 9d–f).

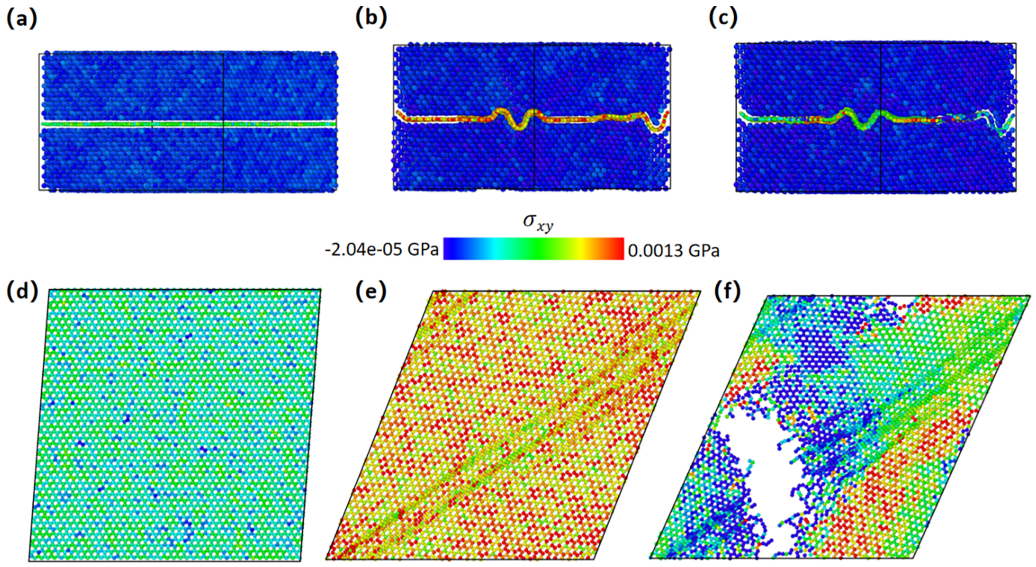

Figure 9: (**a**–**c**) Shear stress distribution in the aluminum-graphene composite material during the shear elastic stage, shear yield stage, and shear failure stage; (**d**–**f**) Stress distribution of the graphene within the composite material during the shear elastic stage, shear yield stage, and shear failure stage.

As shown in Fig. 10, the shear stress–strain curves of Al–graphene composites containing graphene with varying defect areas reveal a clear trend: the overall shear strength of the composites decreases progressively with increasing defect size. This demonstrates that the defect area on the graphene surface exerts a pronounced influence on the shear mechanical performance of Al–graphene composites. An appropriate amount of defects helps strengthen the interfacial bonding effect, whereas excessive defects will destroy the bonding effect [17]; therefore, there exists a critical value for the defect size. As the defect area fraction rises from 1.24% to 13.8%, the shear strength decreases markedly by ~14%–15%. Beyond 13.8%, it drops sharply, which trigger premature fracture.

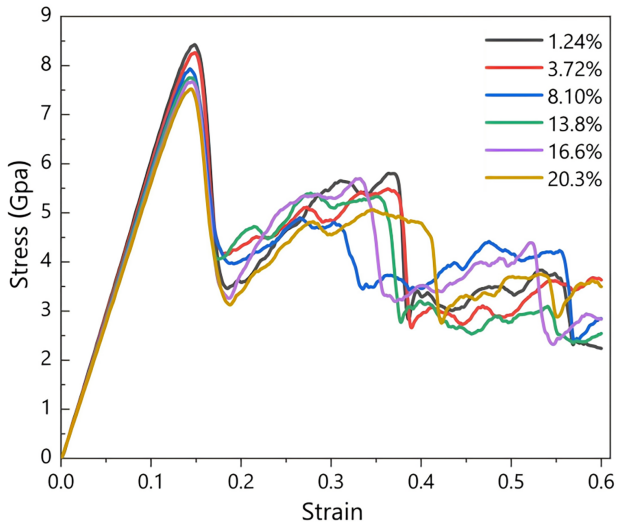

Figure 10: Shear stress-strain curves of Al-graphene composites with graphene containing different defect areas. These composites have the same aluminum matrix volume, but the defective areas in the contained graphene differ. Each curve represents graphene with its respective defect area size (1.24%, 3.72%, 8.10%, 13.8%, 16.6%, and 20.3%).

To elucidate the intrinsic mechanisms underlying the degradation of mechanical performance in Al–graphene composites with defective graphene, a representative model containing a graphene defect area of 13.8% was selected for systematic investigation. The shear stress distribution across different constituent phases was analyzed at various stages of the shear process. As shown in Fig. 11, similar to the defect-free composite, graphene consistently sustains stresses significantly higher than those in the aluminum matrix at any stage of shear deformation, confirming its role as an effective load-transfer medium. However, throughout the shear process, the overall stress borne by defective graphene remains lower than that of pristine graphene (Fig. 9), indicating a markedly reduced load-transfer efficiency.

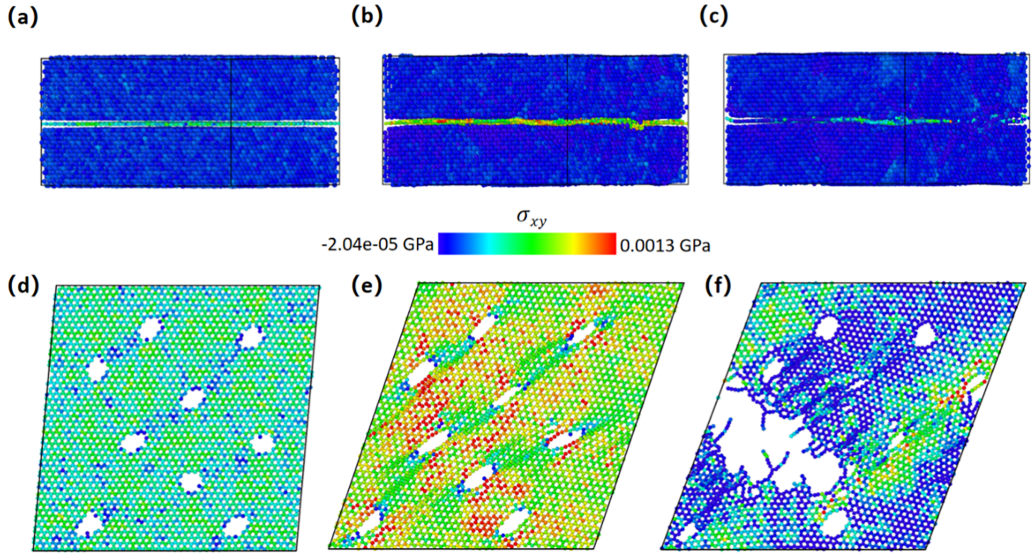

Figure 11: (**a**–**c**) Distribution of shear stress in the Al-graphene composite material containing graphene with 13.8% pore defects, during the shear elastic, yield, and failure stages, respectively; (**d**–**f**) Stress distribution within the defective graphene of the composite material during the corresponding shear elastic, yield, and failure stages.

In the early elastic stage (Fig. 11a,d), atoms surrounding vacancy defects in graphene carry stresses comparable to those in the aluminum matrix, which are substantially lower than those sustained by other carbon atoms. This localized weakening diminishes the efficiency of load transfer. In the subsequent yielding stage prior to fracture (Fig. 11b,e), stress becomes concentrated around the vacancy defects, accelerating crack initiation and propagation between defect sites. As a result, the defective graphene composite fails earlier than its pristine counterpart. In the final failure stage (Fig. 11c,f), immediately after fracture, the stress in graphene rapidly drops to levels comparable to the aluminum matrix, with a faster decline than observed in defect-free graphene (Fig. 9).

Overall, the increase in vacancy defects reduces the effective graphene content within the composite, thereby impairing its ability to transfer load efficiently. This diminished load-transfer capacity directly accounts for the observed reduction in mechanical strength of Al–graphene composites containing defective graphene.

From the onset of shear loading, as shear strain progressively increases, the surface of defective graphene within Al–graphene composites begins to develop buckling waves, with the amplitude of fluctuations intensifying over time. The presence of surface defects destabilizes the graphene lattice, thereby weakening the constraining effect of the aluminum matrix on the reinforcing phase (Fig. 12a,d). As shown in Fig. 12b,e,

the buckling waves and their crests and troughs are predominantly localized around defect sites, where fracture is also more likely to initiate.

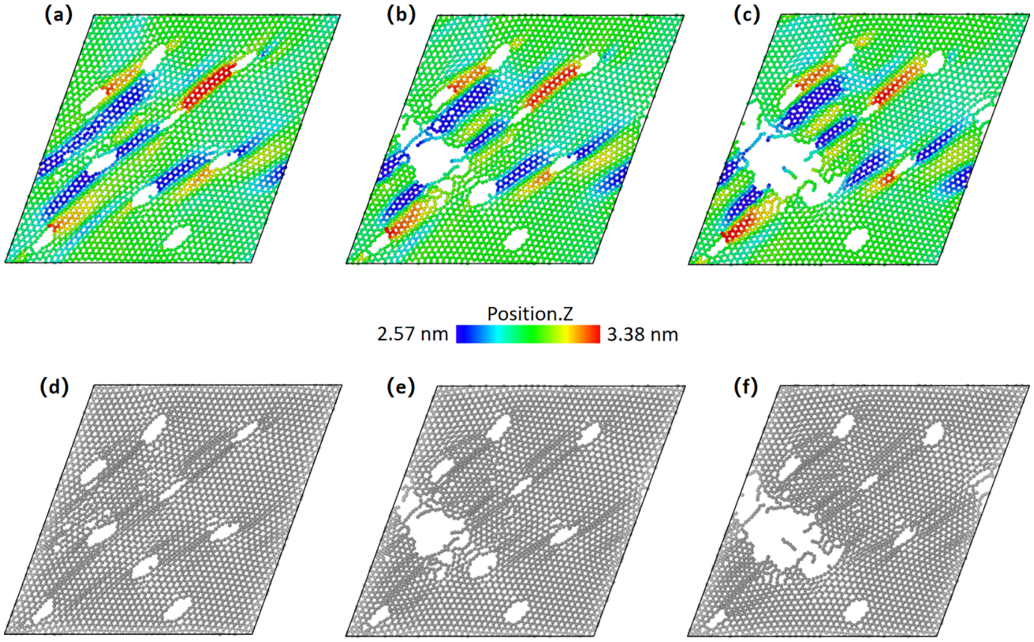

Figure 12: Buckling fracture process of the graphene within the Al-graphene composite material containing graphene with 13.8% pore defects. The color of the atoms in the images (**a**–**c**) represents their different positions along the *Z*-axis. (**d**–**f**) Buckling waves on the graphene atomic surface during the fracture process.

During the final fracture stage of shear deformation, a small crack first nucleates in the vicinity of a graphene defect. The crack then propagates across three consecutive vacancy defects, enlarging the fracture area and ultimately leading to catastrophic failure of the composite (Fig. 12c,f). It should be noted that, limited by the femtosecond timescale of atomic vibrations, the strain rate in our molecular dynamics simulations is higher than that under quasi-static experimental conditions, and a temperature of 0.1 K is applied to avoid thermal fluctuations.

4 Conclusions

This study employs molecular dynamics simulations to investigate the influence of graphene vacancy defects on dislocation–interface interactions and the strengthening and failure mechanisms during shear deformation in Al–graphene composites.

1. During dislocation transmission across the Al–graphene interface, defective graphene exhibits larger buckling amplitudes compared to pristine graphene. However, its buckling periodicity is markedly weakened and eventually vanishes. This is attributed to the reflection, refraction, and mode conversion of buckling waves at defect sites, which render the overall oscillation disordered. Such irregular energy dissipation diminishes the dislocation pile-up strengthening effect, thereby reducing the composite strength.
2. Increased graphene pore defects lower overall shear strength in aluminum matrix composites. During shear deformation, pore defects weaken load transfer efficiency, causing stress concentration at defect edges, amplifying graphene buckling amplitude while disordering waves, ultimately concentrating peaks-valleys near pores and inducing early fracture. Increasing the graphene defect area fraction to

13.8% reduces shear strength by 14%–15% relative to pristine graphene, beyond which reinforcement efficiency declines sharply.

Overall, this work reveals the fundamental role of graphene defects in governing dislocation dynamics and shear-induced failure at Al–graphene interfaces. The findings provide theoretical guidance for the design and optimization of high-performance Al-graphene composites in the engineering applications. It is worth noting that in reality, graphene-reinforced aluminum matrix composites exist only in the form of aluminum alloys, rather than pure aluminum, and the effects of their alloying elements on mechanical properties require further investigation.

Acknowledgement: Not applicable.

Funding Statement: Simulations were performed at Guangdong Province Engineering Research Center of Metal Matrix Composite Database (Institute of New Materials, Guangdong Academic of Science). This work was financially supported by National Key R&D Program of China (2024YFE0109100).

Author Contributions: Junzhe Zhao: Writing—review & editing, Writing—original draft, Methodology, Investigation, Formal analysis. Wencan Zhu: Writing—review & editing, Writing—original draft, Methodology, Investigation, Formal analysis. Qiang Wang: Writing—review & editing. Hui Chen: Conceptualization. Yan Liu: Writing—review & editing, Formal analysis. Kaihong Zheng: Funding acquisition. Zhibo Zhang: Writing—review & editing, Supervision, Funding acquisition, Conceptualization. All authors reviewed and approved the final version of the manuscript.

Availability of Data and Materials: Data available on request from the authors. The data that support the findings of this study are available from the Corresponding Author, [Zhibo Zhang], upon reasonable request.

Ethics Approval: Not applicable.

Conflicts of Interest: The authors declare no conflicts of interest.

References

1. Chen D, Li J, Sun K, Fan J. Graphene-reinforced metal matrix composites: fabrication, properties, and challenges. Int J Adv Manuf Technol. 2023;125(7):2925–65. doi:10.1007/s00170-023-10886-4.
2. Dahiya M, Khanna V, Anil Bansal S. Aluminium-graphene metal matrix nanocomposites: modelling, analysis, and simulation approach to estimate mechanical properties. Mater Today Proc. 2023;78(5696):414–9. doi:10.1016/j.matpr.2022.10.181.
3. Hasan MS, Wong T, Rohatgi PK, Nosonovsky M. Analysis of the friction and wear of graphene reinforced aluminum metal matrix composites using machine learning models. Tribol Int. 2022;170(1):107527. doi:10.1016/j.triboint.2022.107527.
4. Lin F, Ren M, Zhu L, Jia F, Jiang Z. Graphene-reinforced aluminium matrix Nanocomposites: fabrication, properties and applications. Adv Nanocompos. 2025;2(1):59–85. doi:10.1016/j.adna.2024.12.001.
5. Liu B, Sun J, Zhao J, Yun X. Hybrid graphene and carbon nanotube-reinforced composites: polymer, metal, and ceramic matrices. Adv Compos Hybrid Mater. 2024;8(1):1. doi:10.1007/s42114-024-01074-3.
6. Lin Y, Watson KA, Kim JW, Baggett DW, Working DC, Connell JW. Bulk preparation of holey graphene via controlled catalytic oxidation. Nanoscale. 2013;5(17):7814–24. doi:10.1039/c3nr02135a.
7. Robertson AW, Allen CS, Wu YA, He K, Olivier J, Neethling J, et al. Spatial control of defect creation in graphene at the nanoscale. Nat Commun. 2012;3(1):1144. doi:10.1038/ncomms2141.
8. Lahiri J, Lin Y, Bozkurt P, Oleynik II, Batzill M. An extended defect in graphene as a metallic wire. Nat Nanotechnol. 2010;5(5):326–9. doi:10.1038/nnano.2010.53.
9. Lusk MT, Carr LD. Nanoengineering defect structures on graphene. Phys Rev Lett. 2008;100(17):175503. doi:10.1103/PhysRevLett.100.175503.

10. Tiwari SK, Pandey SK, Pandey R, Wang N, Bystrzejewski M, Mishra YK, et al. Stone–Wales defect in graphene. Small. 2023;19(44):2303340. doi:10.1002/smll.202303340.
11. Wei Y, Wu J, Yin H, Shi X, Yang R, Dresselhaus M. The nature of strength enhancement and weakening by pentagon-heptagon defects in graphene. Nat Mater. 2012;11(9):759–63. doi:10.1038/nmat3370.
12. Klein BP, Ihle A, Kachel SR, Ruppenthal L, Hall SJ, Sattler L, et al. Topological stone–Wales defects enhance bonding and electronic coupling at the graphene/metal interface. ACS Nano. 2022;16(8):11979–87. doi:10.1021/acsnano.2c01952.
13. Guarda C, Faria B, Silvestre N, Canongia Lopes JN. Influence of matrix recrystallization and nanofiller porosity on the interfacial properties of holey graphene-aluminium nanocomposites. Compos Struct. 2023;312(1):116856. doi:10.1016/j.compstruct.2023.116856.
14. Wales DJ. Chemistry, geometry, and defects in two dimensions. ACS Nano. 2014;8(2):1081–5.
15. Shin SE, Choi HJ, Shin JH, Bae DH. Strengthening behavior of few-layered graphene/aluminum composites. Carbon. 2015;82(4):143–51. doi:10.1016/j.carbon.2014.10.044.
16. Liao Y, Li Z, Chen L, Croll AB, Xia W. Crumpling defective graphene sheets. Nano Lett. 2023;23(8):3637–44. doi:10.1021/acs.nanolett.2c04771.
17. Li Z, Zhang Y, Zhang Z, Cui YT, Guo Q, Liu P, et al. A nanodispersion-in-nanograins strategy for ultra-strong, ductile and stable metal nanocomposites. Nat Commun. 2022;13(1):5581. doi:10.1038/s41467-022-33261-5.
18. Li Z, Fu X, Guo Q, Zhao L, Fan G, Li Z, et al. Graphene quality dominated interface deformation behavior of graphene-metal composite: the defective is better. Int J Plast. 2018;111:253–65. doi:10.1016/j.ijplas.2018.07.020.
19. Jin ZH, Gumbsch P, Ma E, Albe K, Lu K, Hahn H, et al. The interaction mechanism of screw dislocations with coherent twin boundaries in different face-centred cubic metals. Scr Mater. 2006;54(6):1163–8. doi:10.1016/j.scriptamat.2005.11.072.
20. Wang L, Jin J, Cao J, Yang P, Peng Q. Interaction of edge dislocations with graphene nanosheets in graphene/Fe composites. Crystals. 2018;8(4):160. doi:10.3390/cryst8040160.
21. Zhu JQ, Yang QS, He XQ, Fu KK. Micro-mechanism of interfacial separation and slippage of graphene/aluminum nanolaminated composites. Nanomater. 2018;8(12):1046. doi:10.3390/nano8121046.
22. Qiu Z, Zhang Z, Xiong Y, Luo X, Li Z, Zheng K, et al. Size effects of graphene sheets on the strengthening mechanism of Al-graphene composites: a molecular dynamics study. Appl Surf Sci. 2022;596(5934):153546. doi:10.1016/j.apsusc.2022.153546.
23. Zhang Z, Urbassek HM. Dislocation-based strengthening mechanisms in metal-matrix nanocomposites: a molecular dynamics study of the influence of reinforcement shape in the Al-Si system. Comput Mater Sci. 2018;145:109–15. doi:10.1016/j.commatsci.2017.12.063.
24. Zhang Z, Urbassek HM. Dislocations penetrating an Al/Si interface. AIP Adv. 2017;7(12):125119. doi:10.1063/1.5008886.
25. Zhang Z, Urbassek HM. Indentation into an Al/Si composite: enhanced dislocation mobility at interface. J Mater Sci. 2018;53(1):799–813. doi:10.1007/s10853-017-1495-6.
26. Zhang Z, Alabd Alhafez I, Urbassek HM. Scratching an Al/Si interface: molecular dynamics study of a composite material. Tribol Lett. 2018;66(3):86. doi:10.1007/s11249-018-1038-6.
27. Luo X, Zhang Z, Chen L, Xiong Y, Shu Y, He J, et al. The near-surface microstructural evolution and the influence of Si particles during nanoscratching of nanocrystalline Al. Appl Surf Sci. 2022;573:151533. doi:10.1016/j.apsusc.2021.151533.
28. Plimpton S. Fast parallel algorithms for short-range molecular dynamics. J Comput Phys. 1995;117(1):1–19. doi:10.1006/jcph.1995.1039.
29. Stukowski A, Albe K. Extracting dislocations and non-dislocation crystal defects from atomistic simulation data. Model Simul Mater Sci Eng. 2010;18(8):085001. doi:10.1088/0965-0393/18/8/085001.
30. Faken D, Jónsson H. Systematic analysis of local atomic structure combined with 3D computer graphics. Comput Mater Sci. 1994;2(2):279–86. doi:10.1016/0927-0256(94)90109-0.
31. Stukowski A, Bulatov VV, Arsenlis A. Automated identification and indexing of dislocations in crystal interfaces. Model Simul Mater Sci Eng. 2012;20(8):085007. doi:10.1088/0965-0393/20/8/085007.

32. Barman S, Gupta KK, Dey S. Molecular dynamics-based explanation of the reinforcement geometry effects on CNT/graphene-reinforced $Al_{0.3}$CoCrFeNi high-entropy alloys. Sci Rep. 2025;15(1):24984. doi:10.1038/s41598-025-06470-3.
33. Yan X, Cao P, Tao W, Sharma P, Park HS. Atomistic modeling at experimental strain rates and timescales. J Phys D Appl Phys. 2016;49(49):493002. doi:10.1088/0022-3727/49/49/493002.
34. Dhaliwal G, Nair PB, Singh CV. Uncertainty analysis and estimation of robust AIREBO parameters for graphene. Carbon N Y. 2019;142(15):300–10. doi:10.1016/j.carbon.2018.10.020.
35. Daw MS, Baskes MI. Embedded-atom method: derivation and application to impurities, surfaces, and other defects in metals. Phys Rev B. 1984;29(12):6443–53. doi:10.1103/physrevb.29.6443.
36. Hwang B, Kim W, Kim J, Lee S, Lim S, Kim S, et al. Role of graphene in reducing fatigue damage in Cu/Gr nanolayered composite. Nano Lett. 2017;17(8):4740–5. doi:10.1021/acs.nanolett.7b01431.
37. Holzinger A, Neusser G, Austen BJJ, Gamero-Quijano A, Herzog G, Arrigan DWM, et al. Investigation of modified nanopore arrays using FIB/SEM tomography. Faraday Discuss. 2018;210:113–30. doi:10.1039/c8fd00019k.
38. Liu J, Niu R, Gu J, Cabral M, Song M, Liao X. Effect of ion irradiation introduced by focused ion-beam milling on the mechanical behaviour of sub-micron-sized samples. Sci Rep. 2020;10(1):10324. doi:10.1038/s41598-020-66564-y.
39. Zhou X, Liu X, Shang J, Yang Q. Grain-size effect on plastic flow stress of nanolaminated polycrystalline aluminum/graphene composites. Mech Mater. 2020;148:103530. doi:10.1016/j.mechmat.2020.103530.
40. Shuang F, Aifantis KE. Relating the strength of graphene/metal composites to the graphene orientation and position. Scr Mater. 2020;181:70–5. doi:10.1016/j.scriptamat.2020.02.014.